RSC Advances

PAPER

View Article Online
View Journal | View Issue

Cite this: *RSC Adv.*, 2025, **15**, 47464

First principles study of multifunctional properties of Ga- and Tl-based quaternary materials for energy applications

Mohannad Al-Hmoud,[a] Banat Gul,[b] Muhammad Salman Khan, *[cd] Siti Maisarah Aziz,[d] Ghlamallah Benabdellah[e] and Ayed M. Binzowaimil[a]

Received 18th September 2025
Accepted 19th November 2025

DOI: 10.1039/d5ra07070h

rsc.li/rsc-advances

The present study used density functional theory and presents a thorough first principles investigation of the structural, electronic, mechanical, optical, and thermoelectric properties of novel $CaGaCu_3Se_4$ and $CaTlCu_3Se_4$ quaternary chalcogenides. With strong bonding networks and advantageous thermoelectric properties, these materials have a cubic $P\bar{4}3m$ space group. Compared to $CaTlCu_3Se_4$, $CaGaCu_3Se_4$ has a more negative cohesive energy of −5.13 eV per atom and formation energy of −3.97 eV per atom, signifying its greater stability. Due to the Ga and Tl substitution effects on the conduction band nature, the band dispersion profile study demonstrates a direct band gap semiconducting nature at the Γ-point, with $CaGaCu_3Se_4$ having a large gap of 1.23 eV and $CaTlCu_3Se_4$ having a gap of 0.31 eV using the TB-mBJ approach. $CaTlCu_3Se_4$ shows an improved low-energy absorption, large static dielectric constant (6.0), and sharper $\varepsilon_2(\omega)$ transitions, while the optical investigation discloses a strong visible-UV absorption and a substantial dielectric response. Both these materials are mechanically strong and ductile, with Pugh's ratios greater than 2.8 and a moderate anisotropic value ($A = 1.3$). $CaGaCu_3Se_4$ gives larger stiffness with $E = 94.94$ GPa and $G = 34.67$ GPa, while $CaTlCu_3Se_4$ shows an improved shear agreement. $CaTlCu_3Se_4$ is a better performer according to the thermoelectric calculations. However, being more conductive, $CaGaCu_3Se_4$ loses more heat because of the greater κ_e. $CaTlCu_3Se_4$ displays promise as a good thermoelectric candidate for energy-conversion applications requiring mid-to-high temperatures.

1. Introduction

Metal chalcogenides are considered remarkable because of their intricate chemistry and diverse structures.[1–3] Cu-based sulphides and selenides have a strong visible light absorption and an appropriate thermoelectric figure of merit.[4–7] A solution-based method to generate monodispersed $Cu_2CdSnSe_4$ nanocrystals was employed, and their thermoelectric capabilities were explored.[8] Notably, chalcogenides containing copper are more common in the Earth's crust and are less expensive.[9–12] Materials that have limited thermal conductivity are useful as efficient thermoelectric components in applications that include storage systems and heat glazes.[13] Changes in cation doping and stoichiometric composition have accelerated advancements in this sector. Variations from ideal stoichiometry, referred to as non-stoichiometry, result in the higher substitutions of Cu atoms at the B or C sites in $Cu_2B(II)C(IV)Se_4$. The addition of extra Cu is driven specifically by two significant factors aimed at increasing the electrical resistance. First, excessive Cu doping will produce more holes because the valence state of Cu in the stoichiometric $Cu_2B(II)C(IV)Se_4$ is +1, which is lower than the valence states of B(II) or C(IV).[14] Second, high Cu doping transforms insulating channels into conducting ones. Cu_2Se_4 and $BCSe_4$ tetrahedral arrays can be regarded as part of the $Cu_2B(II)C(IV)Se_4$ crystal structure. Cu_2Se_4 may improve electrical conduction channels within the crystal lattice by replacing the Cu with B(II) and C(IV) elements, lowering electrical resistance.[15] In a study by Liu *et al.*,[16] undoped $Cu_2CdSnSe_4$ possessed an electrical conductivity of about 0.31×10^4 S m^{-1}, and small amounts of Cu doping enhanced it to 1.89×10^4 S m^{-1}, resulting in a six-fold rise. Heavy Cu doping significantly raised the carrier concentration in the $Cu_2MnSnSe_4$ system, from 0.21×10^{20} to 2.89×10^{20} cm^{-3}. The *ZT*s of quaternary chalcogenides increase with a change in thermal conductivity. The ZT_{max} for $Cu_{2.1}Cd_{0.9}SnSe_4$ is approximately 0.7, whereas it is 0.4 for undoped $Cu_2CdSnSe_4$.[17] Because of the excellent crystal structure of $Cu_2B(II)C(IV)Se_4$, doping excess Cu into the matrix can dramatically reduce the high electrical

[a]*Department of Physics, College of Science, Imam Mohammad Ibn Saud Islamic University (IMSIU), Riyadh, 13318, Saudi Arabia*
[b]*National University of Sciences and Technology (NUST), Islamabad, Pakistan*
[c]*Department of Physics, Abdul Wali Khan University, Mardan, 23200, Pakistan. E-mail: salmankhan73030@gmail.com*
[d]*UniSZA Science and Medicine Foundation Centre, Universiti Sultan Zainal Abidin, Gong Badak Campus, 21300 Kuala Nerus, Terengganu, Malaysia*
[e]*Laboratory of Physical Engineering, Department of Physic, Faculty of Matter Sciences, University of Tiaret, Algeria*

resistance to a suitable magnitude, resulting in a higher PF. Other examples of this strategy include the Fe cation substitution for Zn and the Ga cation substitution for Sn.[18] Doped samples have greater PFs due to increased electrical conductivity caused by excessive Cu or cation doping.[19]

Sankar *et al.*[20] synthesized four monoclinic (SG *C*2/*c*) quaternary sulphides and selenides with the general formula Tl_2PbMX_4 (M = Zr and Hf; X = Se). In the infrared spectrum, graphs of $BaCu_2GeS_4$ (1.52 eV), $SrCu_2GeS_4$ (1.50 eV), $BaCu_2GeSe_4$ (1.30 eV), and $SrCu_2GeSe_4$ (0.93 eV) indicate a redshift in maximum absorption. These chalcogenides are attractive thermoelectric materials due to their anticipated thermoelectric characteristics. The *ZT* values of XCu_2GeQ_4 (X = Ba and Sr; Q = S and Se) decreased in the following order: $SrCu_2GeSe_4$ (2.6), $BaCu_2GeSe_4$ (1.85), $SrCu_2GeS_4$ (1.01), and $BaCu_2GeS_4$ (0.94).[21] In the study by Issam El Bakkali *et al.*,[22] the physical properties of the chalcogenide compound $TaCu_3X_4$ (X = S, Se, and Te) were investigated by means of first-principles calculations. The band structure analysis revealed that all examined materials were semiconducting, with direct band gaps of 2.4, 2.2, and 2 eV for $TaCu_3X_4$ (X = S, Se, and Te), respectively. Notably, substantial absorption was noticed in both the visible and low UV bands. Additionally, Cu_3TaX_4 (X = S, Se, and Te) materials have been confirmed for usage in ion synaptic transistors, permitting neuromorphic computing for energy-efficient AI systems.[23,24] However, the stability and ecological impact of $TaCu_3X_4$ materials are determined by their chemical durability and degradation impacts under numerous operating conditions.[25] While tellurides are more stable, their toxicity is a concern; sulphides and selenides are prone to oxidation and ion leaching, potentially contaminating the environment. Baghel *et al.*[26] and Wang *et al.*[27] reported comparable issues, highlighting the importance of balancing material performance with sustainability. An investigation was carried out to improve the performance of a Bi-doped p-type Cu_3SbSe_4 thermoelectric material by raising the Ag concentration. Adding Ag generates many secondary phases and defects that scatter phonons, decreasing thermal conductivity while increasing electrical conductivity, which leads to a greater figure of merit (*ZT*) at higher temperatures.[34] Sn-doped Cu_3SbSe_4 thermoelectric compound was developed and its p-type thermoelectric properties are improved. By substituting Sn at the Sb site, an improved carrier concentration (holes) and optimized electrical-to-thermal conductivity ratio were attained, resulting in higher thermoelectric performance.[35] Future applications, principally in the energy and industrial sectors, must inspect both stability and ecological hazards in order to create materials that offer greater performance without causing long-term environmental damage.[28] The study of quaternary chalcogenides has received a lot of attention in recent years because of the intriguing multifunctional features in electronics, optoelectronics, and thermoelectric fields. The electronic structure simulations show semiconducting behavior with an appropriate energy gap, representing the possibility of optoelectronic devices, such as photovoltaics and photodetectors. The mechanical properties, attained from the elastic constants, validate mechanical stability and ductility, which are critical for practical device manufacturing and their durability.

2. Computational details

We studied the electronic, optical, elastic, and thermoelectric properties of $CaGaCu_3Se_4$ and $CaTlCu_3Se_4$ quaternary chalcogenides using the first-principles density functional theory (DFT) employed in the WIEN2k package.[29] To increase the accuracy of band structure and related features, particularly electronic and optical responses, the modified Becke–Johnson (TB-mBJ) potential was used as the exchange-correlation function.[30] The TB-mBJ potential has been shown to produce more consistent energy gap predictions for materials than the typical generalized gradient approximation (GGA) or local density approximation (LDA); hence, it was used for all electronic structure computations in this study.[31] The muffin-tin radii (R_{MT}) were carefully chosen to limit charge leakage while maintaining the overlapping sphere condition, with typical values of roughly 2.5 a.u. for Ca and Tl/Ga atoms and slightly smaller radii for Cu and Se to accommodate their denser electronic configurations. To ensure convergence of the total energy and charge density, the plane wave cutoff was set at $R \times K_{max} = 8.0$. For Brillouin zone sampling, a dense $12 \times 12 \times 12$ *k*-point mesh is used, with further increases for the density of states (DOS) and optical calculations. The strain–stress technique was used to evaluate the mechanical stability and elastic response.[32] Elastic constants (C_{ij}) and other parameters were determined, allowing for the classification of mechanical behavior into ductility, brittleness, and anisotropy. To evaluate thermoelectric performance, the Boltzmann transport relations were solved with the constant relaxation time approximation using the BoltzTraP code.[33] Transport calculations used a rigid band model to replicate doping by altering the chemical potential and were run up to 900 K to simulate high-temperature applications.

3. Results and discussions

3.1. Structural properties

$CaGaCu_3Se_4$ forms a cubic phase with the space group $P\bar{4}3m$ (Fig. 1). Four similar Se^{2-} atoms connect with Ca^{2+} to form the

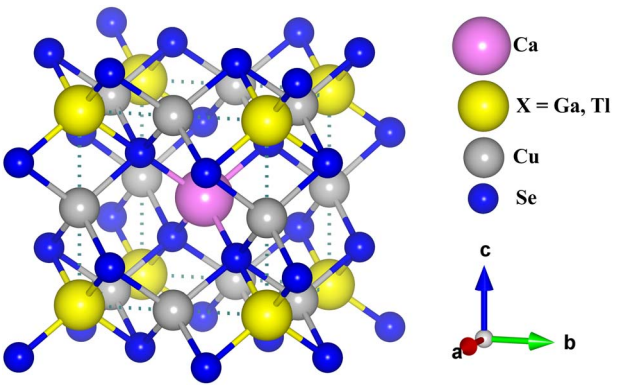

Fig. 1 Unit cell crystal structure of $CaXCu_3Se_4$ (X = Ga and Tl) quaternary chalcogenides.

$CaSe_4$ tetrahedra, which connect corners to four similar $GaSe_4$ tetrahedra and 12 identical $CuSe_4$ tetrahedra. The Ca–Se bonds measure 2.78 Å. Cu^{1+} joins four identical Se^{2-} to form the $CuSe_4$ tetrahedra. They also share edges with the four $CaSe_4$ tetrahedra, with corners connected to eight $CuSe_4$ tetrahedra. The bond lengths between Cu and Se are 2.54 Å each. Four similar Se^{2-} atoms connect with Ga^{3+} to form the $GaSe_4$ tetrahedra. These tetrahedra link corners to four $CaSe_4$ tetrahedra and edges to six $CuSe_4$ tetrahedra. The Ga–Se bonds measure 2.41 Å. The Se^{2-} interacts with one Ca^{2+} atom, three similar Cu^{1+} atoms, and one Ga^{3+} atom to form distorted corner- and edge-sharing trigonal bipyramids ($CaGaCu_3Se_4$). $CaTlCu_3Se_4$ also crystallizes in the cubic $P\bar{4}3m$ space group. $CaSe_4$ tetrahedra are formed when four identical Se^{2-} atoms link with Ca^{2+}. They share corners with four identical $TlSe_4$ tetrahedra and 12 identical $CuSe_4$ tetrahedra. The Cu^{1+} atoms join to 4 similar Se^{2-} atoms, producing $CuSe_4$ tetrahedra. $CaGaCu_3Se_4$ and $CaTlCu_3Se_4$ show the calculated cohesive energy values of −5.13 and −5.04 (eV per atom), respectively (see Table 1), indicating strong interatomic bonding in both materials. A low cohesive energy means more energy gets released during solid formation from isolated atoms, signifying increased structural stability. $CaGaCu_3Se_4$ has a slightly more negative cohesive energy than $CaTlCu_3Se_4$, signifying stronger bonding contacts and a more stable crystal structure. Similarly, the formation energies, which quantify the thermodynamically favorable building of a material from the constituent elements, are −3.97 eV for $CaGaCu_3Se_4$ and −3.85 eV per atom for $CaTlCu_3Se_4$ (see Table 1). The lower the formation energy, the more chemically stable and feasible the synthesis will be. Therefore, $CaGaCu_3Se_4$ is thermodynamically more stable than $CaTlCu_3Se_4$. The difference in energetic favorability is accredited to the inherent character of the component elements. Gallium, being light and generating a stronger directional covalent influence due to its smaller size and high electronegativity, contributes more effectively to cohesive connections than thallium, which is heavy, less electronegative, and produces more dispersed bonds. Additionally, the replacement of Ga with Tl could result in a greater lattice distortion because of the size disparity, substantially weakening the overall bonding. Typical energy–volume (E–V) curves

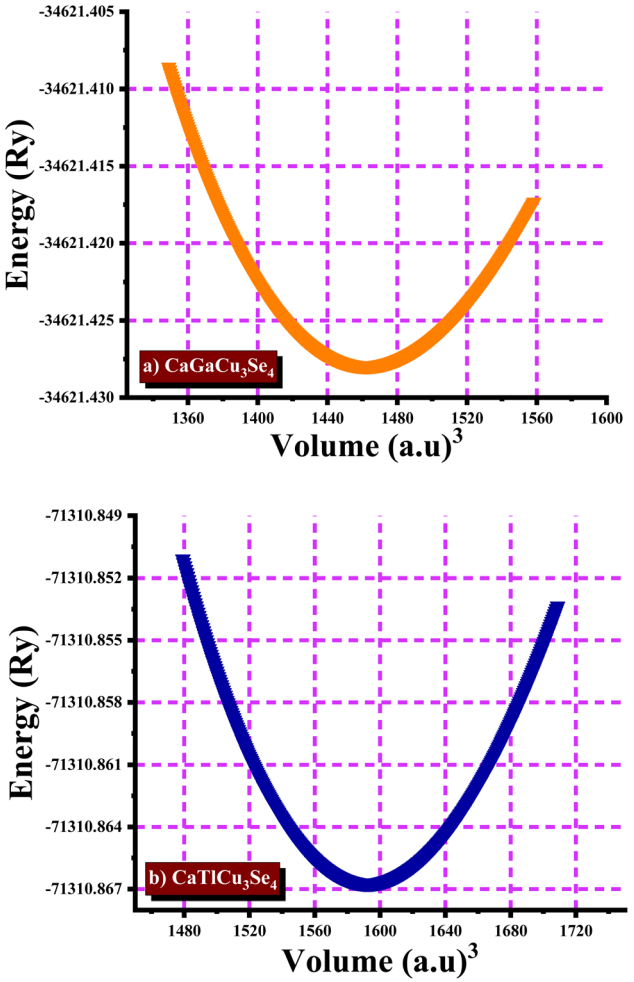

Fig. 2 Optimization curves of $CaGaCu_3Se_4$ and $CaTlCu_3Se_4$ quaternary chalcogenides.

Table 1 Lattice constants, formation and cohesive energies, and energy gaps of $CaXCu_3Se_4$ (X = Ga and Tl) quaternary chalcogenides

Materials	a (Å)	b (Å)	c (Å)	E_g (eV) TB-mBJ	E_g (eV) SOC	E_{form} (eV/f.u)	E_{coh} eV per atom
$CaGaCu_3Se_4$	5.12	5.12	5.12	1.23	1.19	−3.97	−5.13
$CaTlCu_3Se_4$	5.66	5.66	5.66	0.31	0.19	−3.85	−5.04
$TaCu_3Se_4$	5.69[a]			1.65[a]			
KCu_3GeSe_4	6.23[b]			0.77[b]			
$RbCu_3GeSe_4$	6.28[b]			1.08[b]			
$CsCu_3GeSe_4$	6.40[b]			1.36[b]			
$RbCu_3SiSe_4$				1.32[c]			
$RbCu_3GeSe_4$				0.73[c]			
$SrAlCu_3Se_4$				1.5[d]			
$SrGaCu_3Se_4$				1.2[d]			
$BaInCu_3Se_4$				0.6[e]			
$BaTlCu_3Se_4$				0.4[e]			
$Cu_2HgGeSe_4$	5.75[f]		11.08[f]	0.54[f]			
$Cu_2CdGeSe_4$	5.60[g]		10.73[g]	1.29[g]			
$CuZn_2InSe_4$	5.52[h]		10.99[h]	1.5[h]			

[a] Ref. 22. [b] Ref. 36. [c] Ref. 37. [d] Ref. 38. [e] Ref. 39. [f] Ref. 40. [g] Ref. 41. [h] Ref. 42.

(Fig. 2(a and b)) derived from *ab initio* total energy calculations are used to calculate the equilibrium structure characteristics. The curves demonstrate a parabolic relationship, indicating that both materials behave as solids when compressed or expanded. The minima of these curves indicate the equilibrium volume, corresponding to the most energetically favorable structures. $CaTlCu_3Se_4$ has a greater equilibrium volume (1600 a.u.^{3}) than $CaGaCu_3Se_4$ (1440 a.u.^{3}), due to the substitution of Ga (atomic number 31) with heavier and larger Tl (atomic number 81). This is consistent with the periodic pattern, as Tl has a much larger atomic radius, causing lattice expansion. $CaTlCu_3Se_4$ (−7810.867 R_y) has a lower minimum total energy than $CaGaCu_3Se_4$ (−34 621.430 R_y). However, this does not directly indicate comparable stability until normalized per atom due to differences in atomic numbers and electron counts. Notably, the curvature of the parabola in the Tl-based material appears significantly steeper, implying that it may have a greater bulk modulus (*i.e.*, less compressible) than the Ga-based material, but this would require quantitative fitting (*e.g.*, Murnaghan or Birch–Murnaghan EOS) to confirm. Such energy-volume equations are critical for estimating lattice constants, evaluating elastic properties, and comprehending

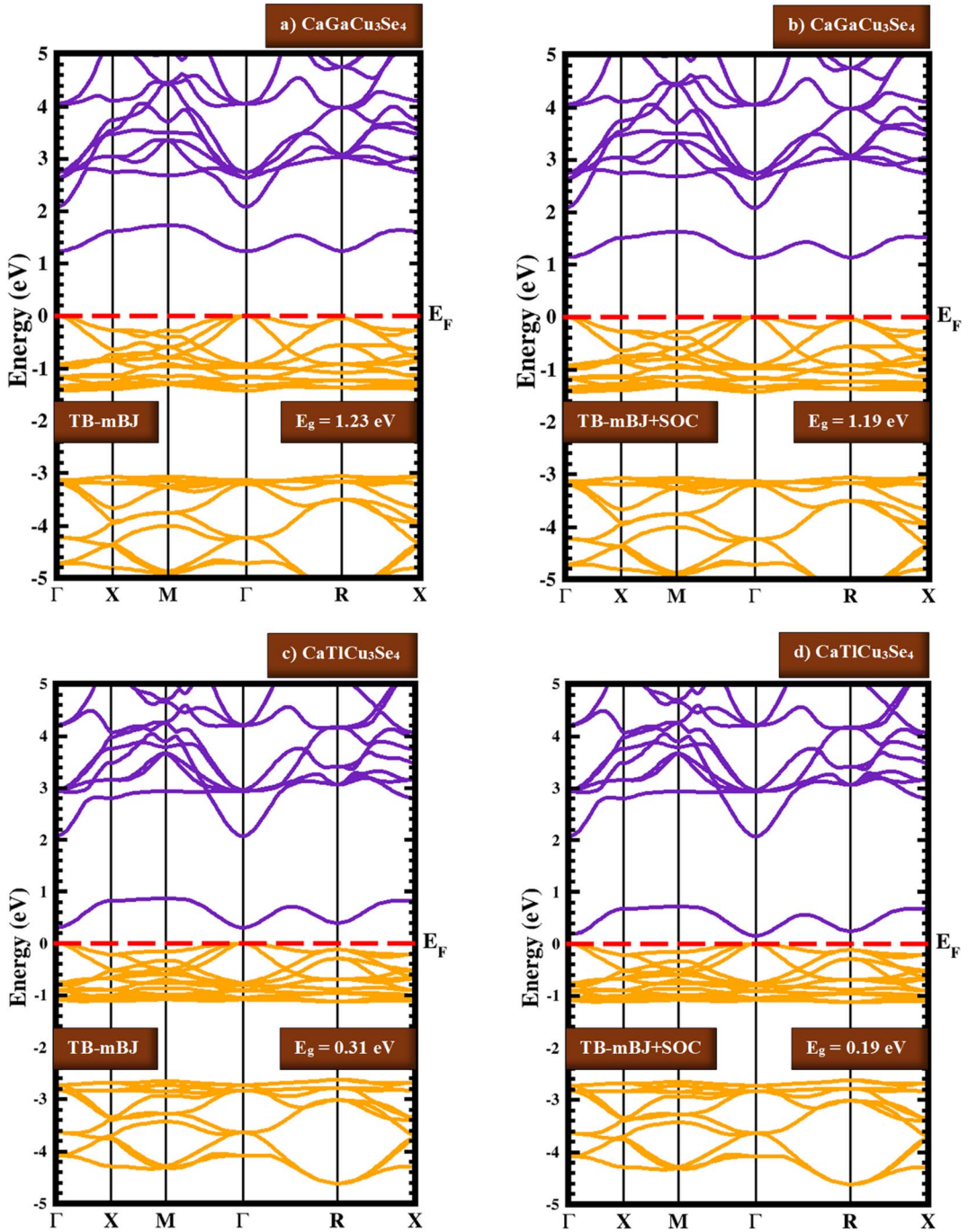

Fig. 3 Electronic band structures (a and b) for $CaGaCu_3Se_4$ and (c and d) for $CaTlCu_3Se_4$ materials by using TB-mBJ and TB-mBJ + SOC.

phase stability, especially in the development of new semiconductors for photovoltaic, thermoelectric, or optoelectronic applications.

3.2. Electronic properties

The electronic band structures of $CaGaCu_3Se_4$ and $CaTlCu_3Se_4$ were predicted (see Fig. 3). Both materials exhibit a direct band gap semiconducting nature, and electrons would move easily from the valence band (VB) to the conduction band (CB) without losing momentum, which is important for optoelectronic devices like light-emitting diodes. The energy gaps calculated using the TB-mBJ scheme for $CaGaCu_3Se_4$ and $CaTlCu_3Se_4$ were 1.23 eV and 0.31 eV, respectively (see Table 1). The variance in energy gaps between $CaGaCu_3Se_4$ (1.23 eV) and $CaTlCu_3Se_4$ (0.31 eV) is mostly because of the substitution of Ga for Tl. Though both Ga and Tl are in group III of the periodic table, they differ significantly in atomic size, electronegativity, orbital character, and relativistic effects, all of which influence the electronic band structure. The TB-mBJ + SOC band structures (see Fig. 3(b) and (d)) reveal a strong, element-dependent impact caused by spin–orbit coupling. The bandgap of $CaGaCu_3Se_4$ is only reduced from 1.23 eV with the TB-mBJ to 1.19 eV with TB-mBJ + SOC, while the relatively small gap of $CaTlCu_3Se_4$ contracts considerably from 0.31 eV to 0.19 eV when SOC is used (see Table 1). In $CaGaCu_3Se_4$, the conduction-band edge is dominated by very light Ga/Cu/Se states (4s/4p and Cu/Se orbitals), which leads to weak relativistic splitting and SOC, resulting in only small band shifts and minimal increase in degeneracies. As a result, the direct Γ–Γ gap remains completely intact and optical/transport properties are only slightly changed. Conversely, $CaTlCu_3Se_4$ has a notable Tl 6s/6p feature near the conduction edge. SOC splits and pushes these Tl-derived bands down in energy, lowering the CBM energy and reducing the gap. SOC-induced band splits in the Tl-based material additionally improve the band curvature and affect effective masses along the band edges, thus increasing carrier concentrations at a particular temperature and changing mobility/Seebeck interactions. The SOC decrease shifts the absorption onset to lower photon energies (redshift), increases low-energy optical activity, and could bring $CaTlCu_3Se_4$ closer to a degenerate semiconductor regime. The observed results clearly demonstrate minimal SOC impact in the Ga-based material and a substantial, performance-specific SOC effect for the Tl-based material. The larger and more widespread 6p orbitals of Tl interact differently with its surrounding Se p and Cu d orbitals than the more focused 4p orbitals of Ga. This results in smaller conduction bands and a low conduction band minimum (CBM) for $CaTlCu_3Se_4$, lowering the band gap. $CaGaCu_3Se_4$ has a large band gap, making it ideal for optoelectronic applications such as solar absorbers and transparent conductors. $CaTlCu_3Se_4$ has a smaller conduction band dispersion, representing a greater effective electron mass. $CaGaCu_3Se_4$ has more conduction bands, signifying delocalized electronic states and lighter carriers, possibly leading to improved carrier mobility. $CaGaCu_3Se_4$ and $CaTlCu_3Se_4$ display substantial variance in the conduction band due to the diverse group III elements. In $CaGaCu_3Se_4$, the Ga-4s states dominate the conduction band edge from 1.5 to 2.0 eV, while in $CaTlCu_3Se_4$, the Tl-6s states dominate between 0.3 and 1.0 eV. The change disturbs optical absorbance and electrical conductivity, potentially making $CaTlCu_3Se_4$ more conductive. Beyond the conduction band edge, Ga-p and Tl-p states contribute to higher energies, changing from 3.0 to 6.0 eV in both materials.

Fig. 4(a and b) shows that the two sets of PDOS and TDOS graphs supplied correspond to two quaternary chalcogenides, $CaGaCu_3Se_4$ and $CaTlCu_3Se_4$. Both materials have comparable stoichiometry and structure, but the substitution of Ga with Tl alters their electronic structures. The TDOS graphs in both plots show the total density of states. These results show that both materials are semiconducting, with discrete band gaps between the valence and conduction bands. In $CaGaCu_3Se_4$, the valence band maximum is predominantly formed by Se-4p and Cu-3d states, with Cu-3d dominating at the Fermi level. Ga contributions originate mostly from the Ga-s/p orbitals in the conduction band, with little presence around the Fermi level. In $CaTlCu_3Se_4$, however, while the Cu-3d and Se-4p orbitals continue to dominate the valence band, Tl introduces new contributions, mainly from the Tl-s and Tl-p states, largely in the conduction band region, with some Tl-d and f contributions as well. Notably, the Tl-f orbitals make no significant contribution near the Fermi level, implying that f-electrons play a negligible role in low-energy excitations. The Cu-3d orbitals impact the VB region in both materials, specifically between −2.0 eV and the Fermi level (0 eV). This suggests that Cu-d states play a substantial role in defining the valence band maximum (VBM) and are likely to influence p-type conduction behavior. The Se-4p states have a substantial impact from −5.0 to −3.0 eV, making bonding states with Cu-d states. The hybridization of Cu-d and Se-p states is prevalent in chalcopyrite-type semiconductors and indicates strong covalent connections. Interestingly, Ga-p and Tl-p orbitals both contribute in the −5.0 to −3.0 eV area, signifying that both Ga and Tl play a role in creating deeper valence band states, but not as strongly as Cu and Se around the Fermi level. In $CaGaCu_3Se_4$ (see Fig. 4(a)), the Ga-s influences from 1.5 to 2.0 eV, demonstrating that Ga-s states have a decent impact in defining the conduction band minimum. In $CaTlCu_3Se_4$, the Tl-s state dominates, although only at lower energies, 0.3 to 1.0 eV, showing that Tl introduces shallower conduction band states than Ga. This energy shift indicates that $CaTlCu_3Se_4$ has a lower band gap, which could make it more conductive or more suited for thermoelectric applications, where narrow band gaps are generally advantageous. Furthermore, the p states of Ga and Tl affect the conduction band at 3.0 eV to 6.0 eV, but they do not influence the CBM as strongly as the s-states. Fig. 4(a and b) reveals that the contribution of Ca (Ca-s and Ca-p) is marginal and dispersed across both valence and conduction regions in both materials, implying a limited role in band-edge creation. This is similar to the typical behavior of Ca in many chalcogenide materials, where its divalent nature aids in charge neutrality, while without significantly altering the electronic band structure.

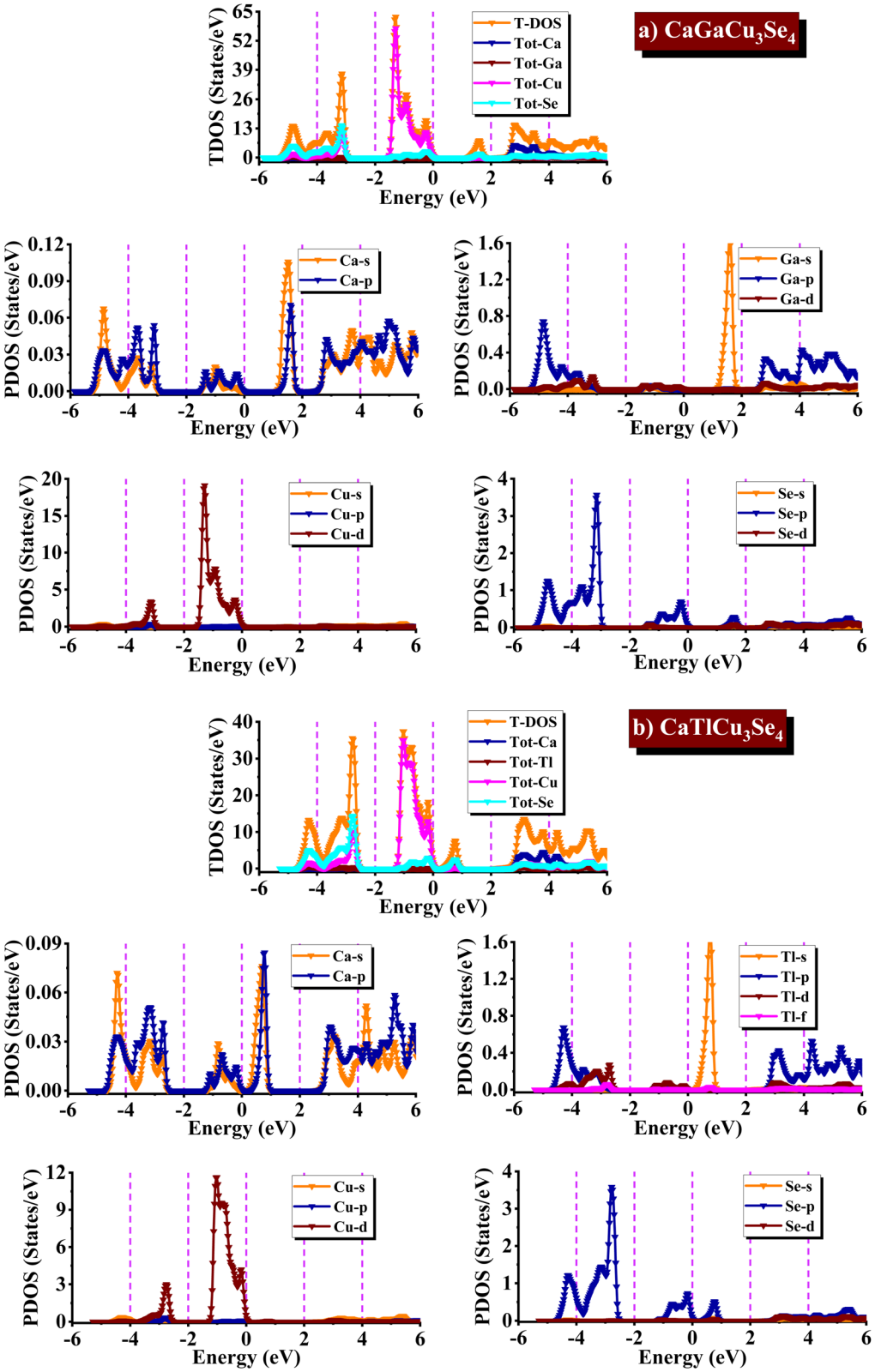

Fig. 4 Calculated density of states of (a) $CaGaCu_3Se_4$ and (b) $CaTlCu_3Se_4$.

3.3. Optical properties

Fig. 5(a) shows the real dielectric function $\varepsilon_1(\omega)$ for $CaGaCu_3Se_4$ and $CaTlCu_3Se_4$. This function reflects the ability of a material to polarize under an external electric field, which is directly related to its electronic polarizability. The static dielectric constants $\varepsilon_1(0)$ (see Table 2) are 5.8 for $CaGaCu_3Se_4$ and 6.0 for $CaTlCu_3Se_4$, demonstrating significantly higher polarizability in

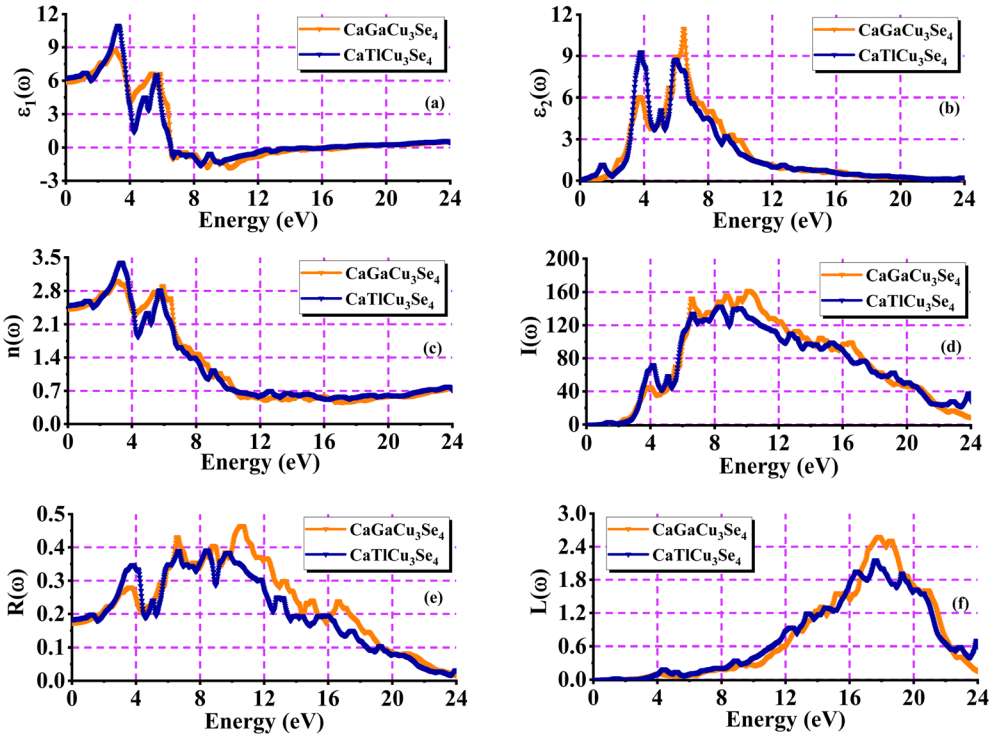

Fig. 5 Calculated (a) real dielectric constant, (b) imaginary dielectric constant, (c) refractive index, (d) absorption coefficient, (e) reflectivity spectra, and (f) electron energy loss function for $CaXCu_3Se_4$ (X = Ga and Tl) quaternary chalcogenides.

the Tl-based material. Both materials show a similar spectral pattern, with $\varepsilon_1(\omega)$ first increasing and reaching a primary peak around 3.5 eV, indicating substantial polarization from low-energy electronic transitions. This is tracked by a depression and a secondary peak at about 5.8 eV, which is the most probable because of supplementary interband transitions or resonance effects. Beyond this threshold, $\varepsilon_1(\omega)$ rapidly decreases and becomes negative at about 6.5 eV, indicating the onset of plasmonic activity or a shift from dielectric to metallic optical response in this energy range. At photon energies above 10.0 eV, $\varepsilon_1(\omega)$ flattens and approaches zero in both materials, representing minimal polarizability and reduced dielectric responsiveness. The similar dielectric behavior of $CaGaCu_3Se_4$ and $CaTlCu_3Se_4$ suggests that substituting Ga with Tl causes only minor changes in dielectric response, thus conserving the overall polarization features, while slightly enhancing the low-energy response in the Tl-based material. Fig. 5(b) shows the imaginary dielectric function $\varepsilon_2(\omega)$ for $CaGaCu_3Se_4$ and $CaTlCu_3Se_4$. This reveals the ability to absorb light through interband electronic transitions. There is substantial difference in the threshold energy of absorption between the two materials. $CaGaCu_3Se_4$ has a threshold at around 1.5 eV, while $CaTlCu_3Se_4$ absorbs the photons at a low energy of 0.5 eV. $CaTlCu_3Se_4$ has a wider optical band gap than $CaGaCu_3Se_4$, permitting it to absorb lower-energy photons with longer wavelengths. This makes it more appropriate for infrared and visible-light applications. Both materials display strong $\varepsilon_2(\omega)$ peaks in the 3.8 to 6.2 eV range, representing intense interband transitions. The strength and location of these peaks specify that the energy range is dynamic for photon absorption and energy conversion procedures. Although both materials have comparable peak positions, $CaTlCu_3Se_4$ has significantly sharper and more intense peaks within this range, representing stronger light-matter interactions and a probable high absorption efficiency in the UV-visible range. Beyond 6.2 eV, the $\varepsilon_2(\omega)$ values of both materials continuously dip, representing the limited availability of electronic states for transitions at higher photon energies. The Tl-based material is optically more active at lower photon energies because of the smaller energy gap.

Table 2 Computed static values of dielectric real component, refractive index, and reflectivity values for $CaXCu_3Se_4$ (X = Ga and Tl) quaternary chalcogenides

Materials	$\varepsilon_1(0)$	$n(0)$	$R(0)$
$CaGaCu_3Se_4$ (this work)	5.8	2.14	0.18
$CaTlCu_3Se_4$ (this work)	6.0	2.15	0.19
$TaCu_3Se_4$		3.12[a]	0.81[a]
KCu_3GeSe_4	5.2[b]	2.30[b]	0.15[b]
$RbCu_3GeSe_4$	5.1[b]	2.25[b]	0.14[b]
$CsCu_3GeSe_4$	5.0[d]	2.23[b]	0.13[b]
$RbCu_3SiSe_4$	5.0[c]	2.0[c]	0.15[c]
$RbCu_3GeSe_4$	4.0[c]	2.3[c]	0.12[c]
$SrAlCu_3Se_4$	5.0[d]	2.23[d]	0.15[d]
$SrGaCu_3Se_4$	6.0[d]	2.50[d]	0.18[d]
$BaInCu_3Se_4$	0.52[e]	2.31[e]	0.15[e]
$BaTlCu_3Se_4$	0.58[e]	2.37[e]	0.16[e]
$Cu_2CdGeSe_4$	7.50[f]	2.75[f]	0.22[f]

[a] Ref. 22. [b] Ref. 36. [c] Ref. 37. [d] Ref. 38. [e] Ref. 39. [f] Ref. 40.

Fig. 5(c) displays the refractive index, $n(\omega)$, which describes light propagation in a material by representing the decrease in the phase velocity of light relative to vacuum. $CaGaCu_3Se_4$ and $CaTlCu_3Se_4$ display a similar dispersion trend for $n(\omega)$, which steadily increases with the photon energy up to 6.0 eV. $CaGaCu_3Se_4$ has a high static refractive index ($n(0)$), representing stronger interaction with light at low frequencies or longer wavelengths. This could make it more factual in applications demanding high light confinement or strong optical response, such as waveguides or photonic crystals. Beyond 6 eV, the refractive index in both materials begins to steadily reduce, consistent with the observed dispersion tendency, following electronic resonance. This drop corresponds to the region where interband transitions are less prevalent, consequential for weak light-matter interactions. A modest fall in both the peak and the static refractive indices for $CaTlCu_3Se_4$ implies a marginally reduced polarizability and light confinement capacity, possibly due to variations in electronic structure and the density of states instigated by the heavier Tl atom. Fig. 5(d) illustrates the absorption coefficient, depicted as $I(\omega)$, that can regulate the depth to which light of a certain energy can spread before being absorbed in the material. This feature is vital for defining a material's pertinency for optical applications like solar cells, photodetectors, and UV absorbers. $CaGaCu_3Se_4$ and $CaTlCu_3Se_4$ have significant UV absorption, mainly above 2.5 eV. $CaTlCu_3Se_4$ has a slightly lower absorption onset, presenting an optical band gap compared to $CaGaCu_3Se_4$. This suggests that Tl substitution reduces the band gap and allows for the absorption of lower-energy (longer-wavelength) photons. Beyond 10.0 eV, $I(\omega)$ quickly declines for both materials, representing fewer possible electronic transitions and worse absorption effectiveness at higher photon energies. The greater absorption in $CaTlCu_3Se_4$ suggests that Tl inclusion improves optical activity, presumably through changes in electronic properties.

The reflectivity $R(\omega)$, a measure of the percentage of incident light that is reflected off the material surface, is shown in Fig. 5(e). The material's optical surface reactivity and suitability for reflecting coatings or photonic devices are determined by this factor. From 3.5 to 11.0 eV, $CaGaCu_3Se_4$ and $CaTlCu_3Se_4$ exhibit notable reflectivity, signifying strong optical activity and high values for additional optical parameters. This indicates that electromagnetic radiation in the UV and deep-UV spectrum interacts strongly with these materials. The materials' reflectivity decreases gradually beyond 11.0 eV, suggesting a decrease in interaction with higher-energy photons as interband transitions become less common. This drop suggests that both compounds become more transparent to extremely high-energy radiation, as it correlates with a fall in the absorption coefficient and $\varepsilon_2(\omega)$ in the same energy range. While the minor modifications brought about by the substitution of Ga and Tl show how small compositional changes can affect optical surface behavior, the similarities in reflectivity patterns verify their structural and electrical harmony. The energy loss function $L(\omega)$, which shows the energy lost by moving electrons as they pass through a system, is displayed in Fig. 5(f). This value is essential for understanding collective electron excitations and plasma oscillations. The $L(\omega)$ of $CaGaCu_3Se_4$ and $CaTlCu_3Se_4$ exhibits high peaks at approximately 18.0 eV and 17.5 eV, respectively. Bulk plasmon excitations are the highest at the plasma resonance frequency, which is linked to these peaks. Due to the replacement of the heavier Tl atom for Ga, the somewhat smaller plasmon peak in $CaTlCu_3Se_4$ suggests a modest shift in dielectric behavior or a marginal decrease in electron density. $CaGaCu_3Se_4$ has a greater peak energy, indicating stronger confinement of free carriers. $CaTlCu_3Se_4$ has a smaller peak, which may provide advantages in tailoring the plasmon response for certain applications.

3.4. Elastic properties

$CaGaCu_3Se_4$ has slightly greater primary stiffness coefficients (C_{11}, C_{12}, and C_{44}) compared to $CaTlCu_3Se_4$ (117.69, 80.97, and 41.71 GPa) (see Table 3). The C_{11} value represents resistance to longitudinal strain in the basic crystallographic direction. The Ga-based combination has a comparatively greater response to uniaxial compression. $CaGaCu_3Se_4$ has a slightly greater resistance to shear deformation, evidenced by the difference in C_{12} and C_{44}. These findings all hint at enhanced inherent stiffness in the Ga-containing compound. The bulk modulus for $CaGaCu_3Se_4$ is 100.13 GPa, while $CaTlCu_3Se_4$ has a value that is slightly lower at 93.21 GPa. These results demonstrate that both materials are generally incompressible; nevertheless, the inclusion of Ga enhances the general packing strength. The shear modulus regulates the resistance to shape change and is a significant parameter in determining stiffness. $CaGaCu_3Se_4$ has a comparatively greater shear modulus of 34.67 GPa, more than $CaTlCu_3Se_4$ with a value of 32.05 GPa, representing its higher stiffness and structural robustness under transverse loads. Young's modulus evaluates stiffness under linear tensile or compressive stress. $CaGaCu_3Se_4$ has a higher value of 94.94 GPa compared to $CaTlCu_3Se_4$, with a value of 88.15 GPa, following the pattern perceived in B and G. The two materials possess Poisson's ratios of around 0.34, suggesting that they expand significantly when compressed. Both materials possess high Pugh's ratios, 2.89 for $CaGaCu_3Se_4$ and 2.91 for

Table 3 Computed elastic coefficients (C_{11}, C_{12}, and C_{44}) elastic moduli, bulk modulus (B), Young's modulus (Y), Poisson's ratio (ν), shear modulus (G), Pugh-ratio, Cauchy pressure (C''), shear constant (C'), and anisotropy constant (A) for $CaXCu_3Se_4$ (X = Ga and Tl) quaternary chalcogenides

Materials	C_{11}	C_{12}	C_{44}	B	Y	ν	G	B/G	C''	C'	A
$CaGaCu_3Se_4$	123.76	88.32	46.34	100.1	94.94	0.343	34.67	2.89	41.98	17.72	1.35
$CaTlCu_3Se_4$	117.69	80.97	41.71	93.2	88.15	0.341	32.05	2.91	39.26	18.36	1.33

$CaTlCu_3Se_4$, representing their ductile character. The slightly higher B/G value for $CaTlCu_3Se_4$ indicates a slightly larger capability for plastic deformation, possibly because of the heavier Tl atom contributing to more flexible bonding networks. Cauchy pressure (C_{12}–C_{44}) is an efficient way to evaluate the nature of atomic bonding. Positive C_p values often indicate metallic bonding and ductility, while negative values indicate brittleness. Both materials had considerably positive values (41.98 GPa for $CaGaCu_3Se_4$ and 39.26 GPa for $CaTlCu_3Se_4$) (see Table 3), demonstrating ductile behavior with a metallic bonding nature. The shear constant provides the resistance to shear deformation. $CaTlCu_3Se_4$ has a slightly higher value (18.36 GPa) compared to $CaGaCu_3Se_4$ (17.72 GPa), which could suggest superior stability under particular shear modes for the Tl-based arrangement, despite its slightly smaller total elastic modulus. A value of 1 signifies elastic isotropy, but values that differ from 1 depict anisotropy. $CaGaCu_3Se_4$ and $CaTlCu_3Se_4$ have slightly greater A values (1.35 and 1.33, respectively) (see Table 3), showing mild elastic anisotropy, with $CaGaCu_3Se_4$ being slightly more anisotropic. $CaGaCu_3Se_4$ and $CaTlCu_3Se_4$ have mechanical stability, ductility, and low anisotropy, which render them suitable for optoelectronic and thermoelectric applications. $CaGaCu_3Se_4$ has better stiffness and shear resistance, but $CaTlCu_3Se_4$ is more ductile and malleable. Some mechanical variations are principally caused by the replacement of Ga with the heavier Tl atom, which alters the bonding nature and packing density. Furthermore, these materials combine structural resilience and mechanical flexibility, which is a rare and desired combination in relevant functional materials.

3.5. Thermoelectric properties

Fig. 6(a–d) compares the thermoelectric characteristics of the two materials, $CaGaCu_3Se_4$ and $CaTlCu_3Se_4$, in the temperature range of 0 K to 700 K. Fig. 6(a) shows the Seebeck coefficient (S), which measures the voltage produced for a temperature

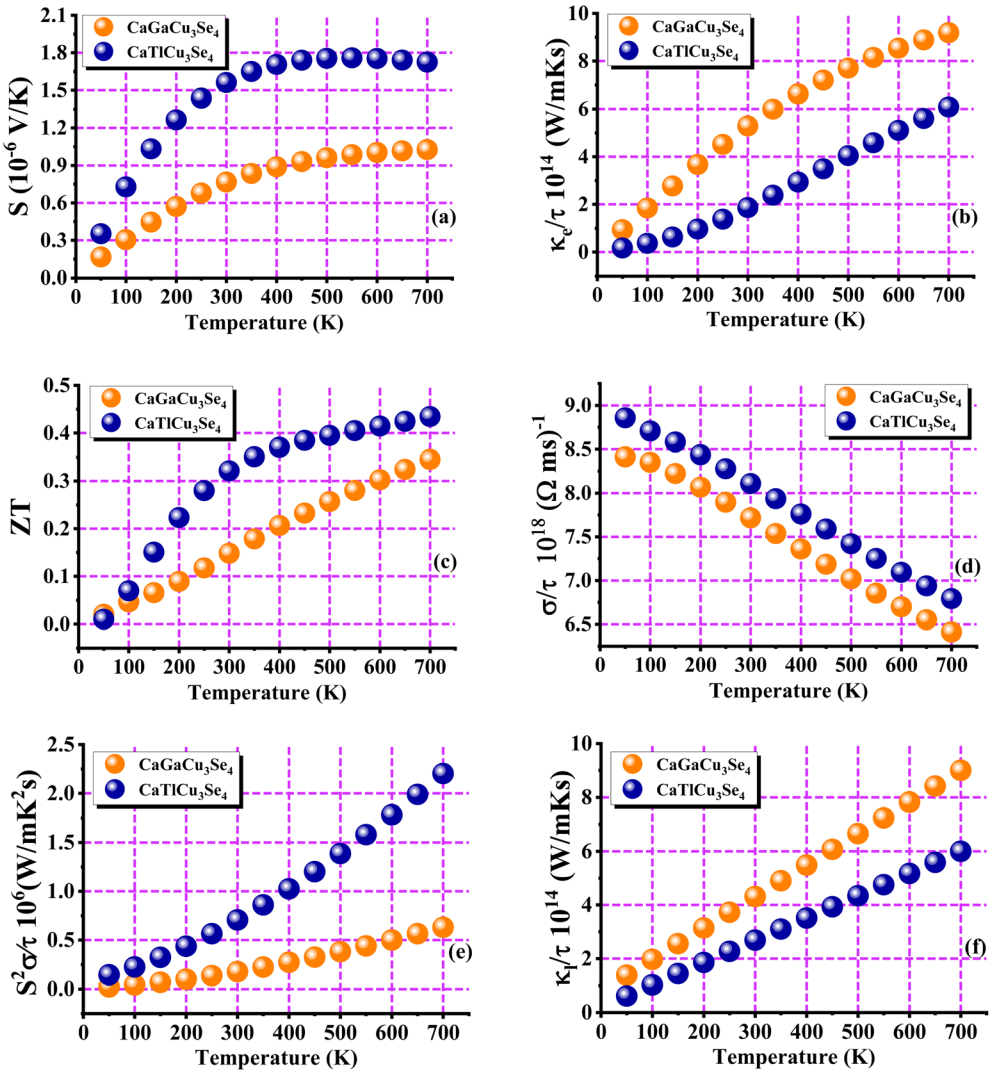

Fig. 6 Calculated (a) Seebeck coefficient, (b) electrical conductivity, (c) figure of merit, (d) electronic thermal conductivity, (e) power factor, and (f) lattice thermal conductivity for $CaXCu_3Se_4$ (X = Ga and Tl) quaternary chalcogenides.

gradient, displayed as a function of temperature for $CaGaCu_3Se_4$ and $CaTlCu_3Se_4$. $CaTlCu_3Se_4$ has a higher S of 0.3 μV K^{-1} at 0 K and gradually increases to 1.80 μV K^{-1} at 700 K. $CaGaCu_3Se_4$ possesses a low initial value of 0.1 μV K^{-1} and gradually increases to 1.0 μV K^{-1} by 700 K. $CaTlCu_3Se_4$ possesses a larger Seebeck coefficient, indicating it can generate more voltage for a given temperature gradient. $CaGaCu_3Se_4$ has probable advantages in electrical conductivity, but its lower Seebeck coefficient restricts its efficiency as a thermoelectric material. Fig. 6(a) shows that $CaTlCu_3Se_4$ has a larger thermopower over the tested temperature range, making it an appropriate choice for applications needing a high Seebeck response. Additionally, the flat increase in S for both materials specifies that carrier scattering mechanisms remain relatively constant with temperature, while intrinsic behavior takes precedence at higher temperatures. $CaTlCu_3Se_4$ suggests a better possibility for thermoelectric applications because of its greater Seebeck coefficient, which measures a material's capacity to convert temperature variations into electrical voltage.

In Fig. 6(b), the electronic thermal conductivity (κ_e) of $CaGaCu_3Se_4$ and $CaTlCu_3Se_4$ is shown as a function of temperature. This demonstrates how charge carriers cause heat transfer in each material. $CaGaCu_3Se_4$ has large κ_e values, commencing at 0.8×10^{14} W m^{-1} K^{-1} s^{-1} at low temperatures and rapidly growing to 9.0×10^{14} W m^{-1} K^{-1} s^{-1} at 700 K. $CaTlCu_3Se_4$ has a slower rise in κ_e, reaching a maximum of 6.0×10^{14} W m^{-1} K^{-1} s^{-1} at 700 K. Charge carriers in $CaGaCu_3Se_4$ carry more thermal energy than those in $CaTlCu_3Se_4$. While high electronic thermal conductivity can be linked to higher electrical conductivity *via* the Wiedemann–Franz law, it is generally undesirable in thermoelectric materials because it allows heat to flow more freely, lowering the temperature gradient and, as a result, thermoelectric efficiency. The low κ_e of $CaTlCu_3Se_4$ is useful since it maintains the temperature differential desirable to drive the Seebeck effect. The quicker rise in κ_e for $CaGaCu_3Se_4$ suggests higher carrier mobility and concentration at higher temperatures. The slight increase in $CaTlCu_3Se_4$ specifies a better balance of electrical performance and thermal insulation. $CaTlCu_3Se_4$ displays low electronic heat conductivity, which increases the thermoelectric performance. The observed inclinations strongly support the assumption that $CaTlCu_3Se_4$ is more proficient for thermoelectric applications, which need a substantial thermal gradient for effective energy conversion. Lower κ_e is recommended for thermoelectric materials as the high thermal conductivity, primarily electronic, can cause heat dissipation instead of energy generation. The small κ_e of $CaTlCu_3Se_4$ expands the thermoelectric performance by maintaining a temperature differential. The projected electronic thermal conductivities at 300 K correspond closely to the previously reported values (see Table 4) for comparable Cu-chalcogenides, especially in terms of magnitude and temperature dependence. This agreement indicates the dependability of our results and confirms the physical reliability of our transport predictions.

Fig. 6(c) reveals the figure of merit (ZT), which is a vital parameter to evaluate thermoelectric performance. $CaTiCu_3Se_4$ exhibits greater ZT values throughout the whole temperature range, which starts near zero at low temperatures and then climbs increasingly to nearly 0.45 at 700 K. $CaGaCu_3Se_4$ has lower ZT values over a similar temperature of roughly 0.32 at 700 K. $CaTiCu_3Se_4$ has the constant gain over $CaGaCu_3Se_4$ because of the greater Seebeck coefficient and lower electronic thermal conductivity. $CaGaCu_3Se_4$ benefits from increased σ, but its relatively low Seebeck coefficient and raised κ_e result in greater heat loss and poorer thermoelectric voltage production, reducing the overall ZT. The consistent increase in ZT with temperature for both materials confirms increased thermoelectric activity at high temperatures, as is typical of many thermoelectric materials. $CaTiCu_3Se_4$ has a higher ZT magnitude across all temperatures, indicating better transport property synergy and higher efficiency as a thermoelectric material. $CaTiCu_3Se_4$ exhibits optimal energy-conversion performance because of its moderate electrical conductivity, high thermopower, and low thermal conductivity. The plot also underlines the significance of limiting heat conductivity over maximizing electrical conductivity, as the latter does not guarantee a high ZT. The projected ZT values for both materials at 300 K (see Table 4) are within the performance range anticipated for Cu-rich chalcogenide thermoelectrics, and they correspond closely to the standard ZT ranges described in prior

Table 4 Computed electrical conductivity, thermal conductivity, and ZT values at 300 K for $CaXCu_3Se_4$ (X = Ga and Tl) quaternary chalcogenides

Materials	Electrical conductivity (10^{18} (Ω ms)$^{-1}$)	Thermal conductivity (10^{14} Wm^{-1} K^{-1} s^{-1})	ZT
$CaGaCu_3Se_4$ (this work)	7.50	5.1	0.15
$CaTlCu_3Se_4$ (this work)	8.10	1.9	0.32
Cu_3SbSe_4	6.0[a]		0.20[a]
$Cu_3SbSnSe_4$	0.9[b]	2.3[b]	0.1[b]
$TaCu_3Se_4$		3.66[c]	1.12[c]
KCu_3GeSe_4	5.0[d]		0.70[d]
$RbCu_3GeSe_4$	1.0[d]		0.65[d]
$CsCu_3GeSe_4$	8.0[d]		0.68[d]
$RbCu_3SiSe_4$		3.0[e]	
$RbCu_3GeSe_4$		5.5[e]	
$SrAlCu_3Se_4$		9.0[f]	0.45[f]

[a] Ref. 34. [b] Ref. 35. [c] Ref. 22. [d] Ref. 36. [e] Ref. 37. [f] Ref. 38.

investigations. This agreement shows that our materials have comparable thermoelectric performance and validates the versatility of our combined electronic and transport approach. Fig. 6(d) illustrates how electrical conductivity (σ) varies with temperature for $CaGaCu_3Se_4$ and $CaTlCu_3Se_4$, measured in 10^{18} $(\Omega\ ms)^{-1}$. Both materials show a decrease in electrical conductivity when the temperature increases, which is typical of metallic and degenerate semiconductors. This trend is mostly because of the increased phonon scattering at high temperatures, which decreases carrier mobility despite relatively steady carrier concentrations. At low temperatures, $CaTlCu_3Se_4$ has a slightly higher electrical conductivity (8.8×10^{18} $(\Omega\ ms)^{-1}$) compared to $CaGaCu_3Se_4$ (8.4×10^{18} $(\Omega\ ms)^{-1}$), indicating a better carrier transport at low thermal agitation. $CaTlCu_3Se_4$ maintains a comparative gain with a conductivity of 6.8×10^{18} $(\Omega\ ms)^{-1}$, while that for $CaGaCu_3Se_4$ drops more prominently to 6.3×10^{18} $(\Omega\ ms)^{-1}$ when the temperature rises to 700 K due to increased phonon scattering. $CaGaCu_3Se_4$ and $CaTlCu_3Se_4$ exhibit electrical conductivity values that match those of comparable Cu-based chalcogenides described in the literature. The consistency demonstrates that our predicted carrier transport behavior is justified and in line with the demonstrated features.

The power factor profiles in Fig. 6(e) for $CaGaCu_3Se_4$ and $CaTlCu_3Se_4$ reveal the different thermoelectric transport features determined by the Seebeck coefficient and electrical conductivity. $CaTlCu_3Se_4$ has a greater PF than $CaGaCu_3Se_4$ at all temperatures. This is due to the larger Seebeck coefficient, which rises rapidly with temperature. $CaGaCu_3Se_4$ begins with a slightly larger electrical conductivity, although balanced by its low thermopower, resulting in a low power factor. As temperatures rise, the power factor of $CaTlCu_3Se_4$ gradually increases, signifying an enhanced energy-filtering performance and a high carrier effective mass at the Fermi level. $CaGaCu_3Se_4$ exhibits a steady increase, representing no improvement in electronic transport properties. The enhancement of the PF of $CaTlCu_3Se_4$ proposes that the Tl substitution advances a desirable band curvature and carrier scattering methods for thermoelectric competence. $CaTlCu_3Se_4$ exceeds $CaGaCu_3Se_4$ in terms of energy conversion efficiency, with roughly two times the power factor at higher temperatures. $CaTlCu_3Se_4$ emerges as the most intriguing thermoelectric system because of its beneficial strong power factor and attractive Seebeck profile. The lattice thermal conductivity (κ_l) was calculated by employing the Slack model, an effective analytical approach for calculating κ_l in crystalline semiconductors and thermoelectric chalcogenides. The Slack model describes κ_l as $\kappa_l = AM\theta_D{}^3\delta/(\gamma^2 n^{2/3} T)$, in which A is a material-dependent constant, M is the average atomic mass, θ_D is the Debye temperature, δ is the atomic volume per atom, γ is the Grüneisen parameter, n is the number of atoms per primitive cell, and T is the temperature. The lattice thermal conductivity (κ_l) behavior, as shown in Fig. 6(e), of $CaGaCu_3Se_4$ and $CaTlCu_3Se_4$ displays their phonon transport effectiveness and the usefulness for thermoelectric applications. $CaTlCu_3Se_4$ reliably displays a decrease in κ_l across the inspected temperature range, a very desirable property as the reduced lattice transport holds the thermal gradient that is needed for operative thermoelectric conversion. The low κ_l of $CaTlCu_3Se_4$ is because of the heavy Tl atoms, which increase mass fluctuation and the anharmonicity through the lattice. These factors prevent the phonon propagation more efficiently than in $CaGaCu_3Se_4$, while the Ga's small mass causes a high κ_l. As temperature increases, Umklapp scattering rises, decreasing κ_l. However, $CaTlCu_3Se_4$ displays a more notable reduction, which leads to a greater performance disparity. $CaGaCu_3Se_4$, however, is structurally a solid, and has a larger κ_l, dropping its overall ZT in spite of its good electrical conductivity. $CaTlCu_3Se_4$ has a higher thermoelectric performance than $CaGaCu_3Se_4$ because of its better balance of phonon and electron transport.

4. Conclusions

This comprehensive first-principles study evaluated the multifunctional features of two novel quaternary chalcogenides, $CaGaCu_3Se_4$ and $CaTlCu_3Se_4$, which are vital for energy applications. Both materials crystallize in the cubic $P\bar{4}3m$ space group with strong frameworks of corner- and edge-sharing tetrahedra, displaying negative cohesive energies of −5.13 eV per atom for $CaGaCu_3Se_4$ and -5.04 eV per atom for $CaTlCu_3Se_4$, together with suitable formation energy values of −3.97 and −3.85 eV per atom, respectively, showing solid interatomic bonding and thermodynamic stability, with $CaGaCu_3Se_4$ being more stable. Electronically, both materials display direct band gaps at the high symmetry Γ-point. $CaGaCu_3Se_4$ exhibits a wider energy gap of 1.23 eV, useful for optoelectronics, while $CaTlCu_3Se_4$, with a small energy gap of 0.31 eV, is appropriate for thermoelectric applications. $CaTlCu_3Se_4$ shows a strong absorption in the visible-UV range, along with higher dielectric constants, sharper $\varepsilon_2(\omega)$ peaks, and lower absorption thresholds, indicating better light-harvesting capabilities. Both materials are elastically stable and ductile, with $CaGaCu_3Se_4$ possessing stronger stiffness ($B = 100.13$ GPa, $G = 34.67$ GPa) and $CaTlCu_3Se_4$ exhibiting more malleability and a slightly higher Pugh's ratio of around 2.91. $CaTlCu_3Se_4$ exhibits a large Seebeck coefficient value of 1.80 μV K^{-1} at 700 K, lower electronic thermal conductivity, and a ZT value of 0.45, compared with 0.32 for $CaGaCu_3Se_4$. This is because of the optimized carrier scattering and the energy filtering outcome. The results display that $CaGaCu_3Se_4$ has mechanical strength and a wider energy gap optoelectronic compensation, while $CaTlCu_3Se_4$ performs well in thermoelectric efficiency and low-energy optical absorption, making them capable for collective energy harvesting technologies.

Conflicts of interest

There are no conflicts to declare.

Data availability

Data are available from the corresponding author upon request.

Acknowledgements

This work was supported and funded by the Deanship of Scientific Research at Imam Mohammad Ibn Saud Islamic University (IMSIU) (grant number IMSIU-DDRSP2503).

References

1 L. Nian, K. Wu, G. He, Z. Yang and S. Pan, *Inorg. Chem.*, 2018, **57**, 3434–3442.
2 A. Ghosh, A. Biswas, R. Thangavel and G. Udayabhanu, *RSC Adv.*, 2016, **6**, 96025–96034.
3 F.-Y. Qi, M. Shele and M. Baiyin, *Inorg. Chem. Commun.*, 2021, **129**, 108635.
4 A. Ashfaq, J. Jacob, K. Mahmood, K. Mehboob, S. Ikram, A. Ali, N. Amin, S. Hussain and U. Rehman, *Phys. B*, 2021, **602**, 412497.
5 C. Coughlan, M. Ibáñez, O. Dobrozhan, A. Singh, A. Cabot and K. M. Ryan, *Chem. Rev.*, 2017, **117**, 5865–6109.
6 X.-Y. Tian, C.-X. Du, G. ZhaoRi, M. SheLe, Y. Bao and M. Baiyin, *RSC Adv.*, 2020, **10**, 34903–34909.
7 S. Maiti, S. Maiti, A. H. Khan, A. Wolf, D. Dorfs, I. Moreels, F. Schreiber and M. Scheele, *Chem. Mater.*, 2019, **31**, 2443–2449.
8 J.-Y. Park, J. H. Noh, T. N. Mandal, S. H. Im, Y. Jun and S. I. Seok, *RSC Adv.*, 2013, **3**, 24918.
9 T. Hirai, K. Kurata and Y. Takeda, *Solid-State Electron.*, 1967, **10**, 975–981.
10 K. Pal, X. Hua, Y. Xia and C. Wolverton, *ACS Appl. Energy Mater.*, 2019, **3**, 2110–2119.
11 J. Ji, Q. Gu, R. Khenata, F. Guo, Y. Wang, T. Yang and X. Tan, *RSC Adv.*, 2020, **10**, 39731–39738.
12 R. Mondal, Y. B. Singh, A. S. Das, S. Kabi, L. S. Singh and D. Biswas, *Phys. B*, 2021, **612**, 412896.
13 L.-D. Zhao, G. Tan, S. Hao, J. He, Y. Pei, H. Chi, H. Wang, S. Gong, H. Xu, V. P. Dravid, C. Uher, G. J. Snyder, C. Wolverton and M. G. Kanatzidis, *Science*, 2016, **351**, 141–144.
14 Q. Song, P. Qiu, H. Chen, K. Zhao, D. Ren, X. Shi and L. Chen, *ACS Appl. Mater. Interfaces*, 2018, **10**, 10123–10131.
15 Ch. Raju, M. Falmbigl, P. Rogl, X. Yan, E. Bauer, J. Horky, M. Zehetbauer and R. Chandra Mallik, *AIP Adv.*, 2013, **3**, 032106.
16 M. Liu, I. Chen, F. Huang and L. Chen, *Adv. Mater.*, 2009, **21**, 3808–3812.
17 Y. Dong, H. Wang and G. S. Nolas, *Phys. Status Solidi RRL*, 2013, **8**, 61–64.
18 X. Y. Shi, F. Q. Huang, M. L. Liu and L. D. Chen, *Appl. Phys. Lett.*, 2009, **94**, 122103.
19 K. Wei, L. Beauchemin, H. Wang, W. D. Porter, J. Martin and G. S. Nolas, *J. Alloys Compd.*, 2015, **650**, 844–847.
20 C. R. Sankar, A. Assoud and H. Kleinke, *Inorg. Chem.*, 2013, **52**, 13869–13874.
21 M. Abubakr, Z. Abbas, A. Naz, H. M. Khalil, M. A. Khan, H. Kim, K. Khan, M. Ouladsmane, S. Rehman, D. Kim and M. F. Khan, *Opt. Quantum Electron.*, 2023, **55**, 849.
22 I. E. Bakkali, A. Talbi, M. Louzazni, A. Lemnawar and K. Nouneh, *Int. J. Energy Res.*, 2025, **2025**, 7846959.
23 A. Galodé, T. Barbier and F. Gascoin, *Materials*, 2023, **16**, 5941.
24 N. Neophytou, S. Foster, V. Vargiamidis, G. Pennelli and D. Narducci, *Mater. Today Phys.*, 2019, **11**, 100159.
25 H. Joshi, A. Shankar, N. Limbu, M. Ram, A. Laref, P. K. Patra, O. B. Ismailova, L. Zuala, S. Chatterjee and D. P. Rai, *ACS Omega*, 2022, **7**, 19070–19079.
26 N. Baghel and A. Kumar, *Solid State Sci.*, 2025, **160**, 107784.
27 L. Wang, R. Moshwan, N. Yuan, Z. Chen and X. Shi, *Adv. Mater.*, 2025, **37**, 2418280.
28 H. Jeong and S. K. Shin, *Chem. Phys. Lett.*, 2018, **692**, 333–339.
29 P. Blaha, K. Schwarz, F. Tran, R. Laskowski, G. K. H. Madsen and L. D. Marks, *J. Chem. Phys.*, 2020, **152**, 074101.
30 F. Tran, P. Blaha and K. Schwarz, *J. Phys.: Condens. Matter*, 2007, **19**, 196208.
31 J. P. Perdew, K. Burke and M. Ernzerhof, *Phys. Rev. Lett.*, 1996, **77**, 3865–3868.
32 S. F. Pugh, *Lond. Edinb. Dubl. Philos. Mag.*, 1954, **45**, 823–843.
33 G. K. H. Madsen and D. J. Singh, *Comput. Phys. Commun.*, 2006, **175**, 67–71.
34 L. Zhao, J. Yang, Y. Zou, J. Hu, G. Liu, H. Shao, X. Zhang, Z. Shi, S. Hussain and G. Qiao, *J. Alloys Compd.*, 2021, **872**, 159659.
35 R. Bhardwaj, A. Bhattacharya, K. Tyagi, B. Gahtori, N. S. Chauhan, S. Bathula, S. Auluck and A. Dhar, *Mater. Res. Bull.*, 2019, **113**, 38–44.
36 M. Saeed, R. Khan, K. M. Abualnaja, A. M. Ali, K. Batool and G. Murtaza, *Int. J. Energy Res.*, 2025, **2025**, 2992478.
37 M. S. Khan, B. Gul, B. Ahmad, G. Khan, M. D. Albaqami, S. M. Wabaidur, G. Wafa and H. Ahmad, *Mater. Sci. Semicond. Process.*, 2024, **177**, 108353.
38 A. S. Mohamed, B. Gul, M. S. Khan, B. Ahmad, G. Benabdellah, H. Ahmad and F. Abbas, *Chem. Phys. Lett.*, 2024, **850**, 141479.
39 A. S. Mohamed, B. Gul, M. S. Khan, G. Benabdellah, B. Ahmad and H. Ahmad, *Phys. Scr.*, 2024, **99**, 075928.
40 N. Sarmadian, R. Saniz, B. Partoens and D. Lamoen, *Appl. Phys.*, 2016, **120**, 085707.
41 T. V. Vu, A. A. Lavrentyev, B. V. Gabrelian, K. D. Pham, C. V. Nguyen, K. C. Tran, H. L. Luong, M. Batouche, O. V. Parasyuk and O. Y. Khyzhun, *J. Electron. Mater.*, 2018, **48**, 705–715.
42 L. Ma, W. Shi and L. M. Woods, *RSC Adv.*, 2022, **12**, 26648–26656.